$\mathcal{R}$esearch in
$\mathcal{A}$stronomy and
$\mathcal{A}$strophysics

A sample of metal-poor galaxies identified from the LAMOST spectral survey

Yu-Long Gao[1,2], Jian-Hui Lian[1,2], Xu Kong[1,2], Ze-Sen Lin[1,2], Ning Hu[1,2], Hai-Yang Liu[1,2],

En-Ci Wang[1,2], Zi-Huang Cao[3], Yong-Hui Hou[4], Yue-Fei Wang[4] and Yong Zhang[4]

[1] CAS Key Laboratory for Research in Galaxies and Cosmology, Department of Astronomy, University of Science and Technology of China, Hefei 230026, China; *ylgao@mail.ustc.edu.cn; xkong@ustc.edu.cn*

[2] School of Astronomy and Space Science, University of Science and Technology of China, Hefei 230026, China

[3] Key Laboratory of Optical Astronomy, National Astronomical Observatories, Chinese Academy of Sciences, Beijing 100012, China

[4] Nanjing Institute of Astronomical Optics & Technology, National Astronomical Observatories, Chinese Academy of Sciences, Nanjing 210042, China

Abstract We present a sample of 48 metal-poor galaxies at $z < 0.14$ selected from $92\,510$ galaxies in the LAMOST survey. These galaxies are identified by their detection of the auroral emission line [O III]$\lambda4363$ above the 3σ level, which allows a direct measurement of electron temperature and oxygen abundance. The emission line fluxes are corrected for internal dust extinction using the Balmer decrement method. With electron temperature derived from [O III]$\lambda\lambda4959, 5007$/[O III]$\lambda4363$ and electron density from [S II]$\lambda6731$/[S II]$\lambda6717$, we obtain the oxygen abundances in our sample which range from $12 + \log(\text{O/H}) = 7.63$ ($0.09\,Z_\odot$) to 8.46 ($0.6\,Z_\odot$). We find an extremely metal-poor galaxy with $12 + \log(\text{O/H}) = 7.63 \pm 0.01$. With multiband photometric data from FUV to NIR and Hα measurements, we also determine the stellar masses and star formation rates, based on the spectral energy distribution fitting and Hα luminosity, respectively. We find that our galaxies have low and intermediate stellar masses with $6.39 \leq \log(M/M_\odot) \leq 9.27$, and high star formation rates (SFRs) with $-2.18 \leq \log(\text{SFR}/M_\odot\,\text{yr}^{-1}) \leq 1.95$. We also find that the metallicities of our galaxies are consistent with the local T_e-based mass–metallicity relation, while the scatter is about 0.28 dex. Additionally, assuming the coefficient of $\alpha = 0.66$, we find most of our galaxies follow the local mass–metallicity–SFR relation, but a scatter of about 0.24 dex exists, suggesting the mass–metallicity relation is weakly dependent on SFR for those metal-poor galaxies.

Key words: galaxies: abundances — galaxies: evolution — galaxies: starburst — star formation

1 INTRODUCTION

Metal-poor galaxies are less chemically evolved galaxies and provide an ideal laboratory for investigating galaxy properties in extreme conditions (Shi et al. 2005; Lian et al. 2016). Among them, extremely metal-poor galaxies (hereafter XMPGs), defined by their low oxygen abundance with $12 + \log(\text{O/H}) \leq 7.65$ (Kniazev et al. 2003; Pustilnik & Martin 2007; Doyle et al. 2005), are the most promising young galaxy candidates in the local universe

(Izotov & Thuan 2004). These XMPGs are suspected to be primeval galaxies that are undergoing their first major mass assembly at the observed redshift (Kniazev et al. 2003). Studying these extreme objects can improve our understanding about the early stages of galaxy assembly.

The determination for abundance of elements is considered more reliable if the electron temperature T_e can be measured directly, because metallicity is anti-correlated with electron temperature. The electron temperature can be obtained using auroral line ratios, such as

[O III]λ4363/[O III]$\lambda\lambda$4959, 5007. This technique is often called the T_e method (Aller 1984). However, galaxies with metallicities derived from the T_e method with [O III]λ4363 detections above 3σ are extremely rare. To date, only about 174 such objects have been found (Ly et al. 2014, 2016b).

In order to enlarge the sample of metal-poor galaxies with [O III]λ4363 detection, we carry out a systematic search for such objects in LAMOST Data Releases (DR3 and DR4 Q1 and Q2). In Section 2, we present our approach for detecting and measuring nebular emission lines, and the selection criteria used to identify metal-poor galaxies. We describe the determination for dust attenuation properties and the gas-phase oxygen abundances in Section 3. In Section 4, we describe the methods for estimating stellar masses and star formation rates (SFRs), and then compare the mass–metallicity relation (MZR) and mass–metallicity–SFR relation with local T_e-based relation in Section 5. In addition, we discuss our results in the context of other studies in Section 6. Finally, we summarize our main conclusions in Section 7.

Throughout this paper, we adopt a flat cosmology with $\Omega_\Lambda = 0.7$, $\Omega_M = 0.3$ and $H_0 = 70\,\mathrm{km\,s^{-1}\,Mpc^{-1}}$ to determine distance-dependent measurements. For reference, we adopt $12 + \log(\mathrm{O/H})_\odot = 8.69$ (Allende Prieto et al. 2001) for metallicity measurements quoted against the solar value, $Z_\odot$.

2 SAMPLE SELECTION

2.1 LAMOST Dataset

The Large Sky Area Multi-Object Fiber Spectroscopic Telescope (LAMOST, also called the Guo Shou Jing Telescope) is a special reflecting Schmidt telescope with an effective aperture of 4 m and a field of view of $5°$ (Wang et al. 1996; Su & Cui 2004; Zhao et al. 2012; Cui et al. 2012; Luo et al. 2012). It is equipped with 4000 fibers, covering a wavelength range of $3800 - 9000\,\text{Å}$ (Luo et al. 2015) at a resolving power $\mathrm{R} \approx 1800$. The LAMOST Data Release 3 (DR3) and Data Release 4 (DR4) Q1 and Q2, based on previous surveys from October 2011 to February 2016, contain about three million spectra with limiting magnitude of $r \approx 18.5\,\mathrm{mag}$. The LAMOST 1D pipeline classifies spectroscopic targets as galaxies, stars and QSOs by matching against observed SDSS spectral templates, see Luo et al. (2015) for details; 92 510 objects from the LAMOST catalog are spectroscopically classified as galaxies ('OBJTYPE' = 'GALAXY').

2.2 Emission-Line Flux Determination

According to Song et al. (2012) and Luo et al. (2015), LAMOST 1D spectra are extracted from CCD images used by the LAMOST 2D pipeline. The wavelength calibration of each spectrum is accomplished by using arc lamp spectral lines, with an average calibration error of less than 0.02 Å. The accuracy of the relative flux calibration of LAMOST is above 90%.

Assuming a unimodal Gaussian line profile, we obtain fluxes of strong emission lines such as [O II]λ3727, [O III]λ4363, Hβ, [O III]$\lambda\lambda$4959, 5007, Hα and [S II]$\lambda\lambda$6717, 6731 by fitting their line profiles using the IDL package MPFIT (Markwardt et al. 2009). The expected location of emission lines is based on a priori redshift determined by the [O III] line. In addition, to estimate the signal-to-noise ratio (S/N) of emission lines, we follow the calculation method in Ly et al. (2014).

2.3 Sample Selection

Among all galaxies from the LAMOST ExtraGAlactic Surveys (LEGAS), we first select a subsample of metal-poor galaxies with emission line flux ratios [N II]λ6583/Hα $\leq$ 0.1, which yields 665 galaxies. Among them, we identify 237 objects with [O III]λ4363 detection at $\geq 3\sigma$. We inspect these 237 objects visually, and find 73 of them are false detections. We also exclude 115 objects that are H I regions in nearby large galaxies using optical images with SDSS SkyServer[1]. Finally, we check the right ascension and declination of the remaining sources, and note that one object was observed twice by LAMOST. We keep the observation that has better spectral quality.

As a consequence, our final sample consists of 48 galaxies, making up only 0.05% of all the LAMOST galaxies until DR4 Q2. This fraction is nearly the same as in SDSS (Ly et al. 2014). The median S/N of [O III]λ4363 is 6.1. We obtain the Hβ equivalent width (EW) by dividing the Hβ flux by continuum spectral flux intensity, which is assumed to be the average value of observed flux intensities within a 50 Å wide component around the Hβ line. All of the galaxy spectra in our sample show strong emission lines with a median (average) EW of Hβ of 42.9 (53.5) Å. The EW distribution of Hβ is shown in Figure 1.

To exclude possible active galactic nucleus (AGN) contamination, we use the BPT diagram (see Baldwin et al. 1981; Veilleux & Osterbrock 1987; Kewley et al. 2001; Kauffmann et al. 2003).
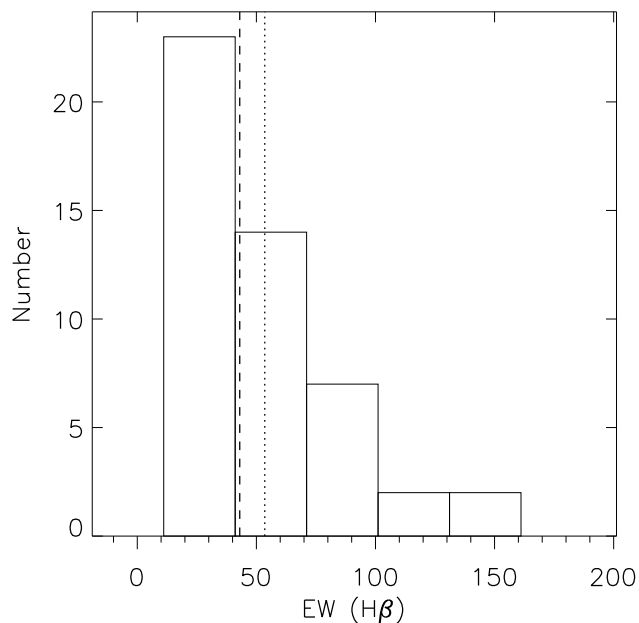
---

[1] *http://skyserver.sdss.org/dr12/en/tools/chart/listinfo.aspx*

Fig. 1 The distribution of Hβ EWs in our sample. The *dashed line* and *dotted line* represent the median and average EWs of 42.9 Å and 53.5 Å, respectively.

Figure 2 shows the distribution of our sample in the BPT diagram. The grayscale 2D histogram shows the number density of LAMOST galaxies. The blue dots represent 48 galaxies in our final sample, and the black crosses represent 24 galaxies in our final sample that have also been spectrally detected by SDSS. Among these 24 galaxies detected with SDSS, 19 galaxy spectra also have [O III]λ4363 detections above 3σ; we will compare these 19 galaxy spectra from LAMOST and SDSS in Section 6.1. The solid and dashed lines are the demarcation curves between star forming galaxies and AGNs derived by Kauffmann et al. (2003) and Kewley et al. (2001). Galaxies located between the two lines are usually classified as composite objects, which may host a mixture of star formation and AGN. It can be seen that all of the galaxies in our final sample are located in the star forming region; however, this is unsurprising since we initially selected sources with [N II]λ6583/H$\alpha \leq 0.1$.

Figure 3 shows example spectra for eight galaxies in our sample that have been spectrally detected by both LAMOST and SDSS. For each object, the left panel shows its LAMOST spectrum, while the right panel shows its SDSS spectrum. All of these spectra exhibit emission lines such as [O II]λ3727 (for all LAMOST spectra and part of the SDSS spectra), Hβ, [O III]$\lambda\lambda$4959, 5007, Hα and [S II]$\lambda\lambda$6717, 6731. The inserted panels feature magnified spectra adjacent to the

[O III]λ4363 lines. It can be seen that weak [O III]λ4363 lines are all detected in the spectra of these galaxies.

3 METALLICITY DETERMINATION

3.1 Dust Attenuation Correction

We correct the emission-line fluxes for internal dust attenuation using Balmer decrement measurements, which estimate the dust extinction by inspecting the change in the Balmer line ratio, such as Hα/Hβ, from its intrinsic value. Generally, the underlying stellar absorption in Balmer lines should be well determined to obtain a reliable emission line measurement (Hu et al. 2016). In this work, we first subtract the underlying stellar continuum and stellar absorption for each spectrum using the STARLIGHT spectral synthesis code (Cid Fernandes et al. 2005). We assume the intrinsic flux ratio of $(H\alpha/H\beta)_0 = 2.86$ (Hummer & Storey 1987) under Case B recombination and use Calzetti et al. (2000) reddening formalism to derive color excesses $E(B-V)$, and then correct the emission line fluxes. In addition, we manually set the color excesses $E(B-V)$ to zero when the Hα/Hβ ratios are less than 2.86.

The resulting reddening-corrected emission line fluxes relative to Hβ and color excesses are listed in Table 1. As shown in panel (a) of Figure 4, the measured dust extinctions are very low with an average $E(B-V)$ value of 0.03 mag.

3.2 Metallicity Calculation

With significant detection of [O III]λ4363, we can determine the metallicity using the so-called T_e method. In this work, we use the python package PYNEB [2] (Luridiana et al. 2015) to calculate electron densities (n_e) and electron temperatures (T_e), which are evolved from the IRAF nebular package (Shaw & Dufour 1995; Shaw et al. 1998). Nicholls et al. (2013) have demonstrated that electron temperatures would be overestimated, and thus the oxygen abundances would be underestimated when using older collision strength data and approximate temperature calibration methods from Izotov et al. (2006). Therefore, we need to set atomic recombination data and atomic collision strength data before the calculation. We adopt atomic recombination data from Froese Fischer & Tachiev (2004) for O^+, O^{++} and Tayal & Zatsarinny (2010) for S^+. For collision strength data, we adopt values from Kisielius et al. (2009) for O^+, Storey et al. (2014) for O^{++} and Tayal & Zatsarinny (2010) for S^+.

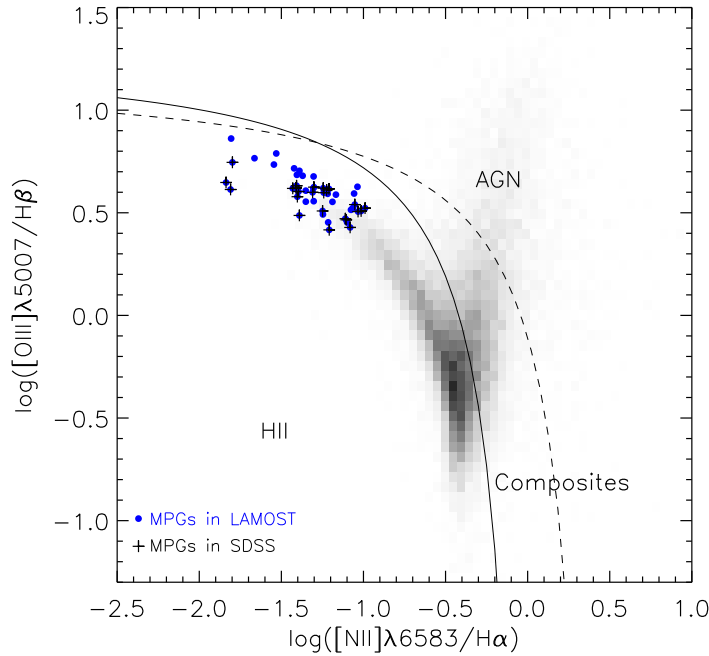[2] *http://www.iac.es/protecto/PyNeb/*

Fig. 2 BPT diagram for our metal-poor galaxy (MPG) sample and all the LAMOST galaxies. The *blue dots* represent our final sample galaxies. The *black crosses* represent these objects in our final sample that have also been spectrally detected with SDSS. The *grayscale 2D histogram* shows the number density of LAMOST galaxies. The *solid* and *dashed lines* are the demarcation curves between star forming galaxies and AGNs defined by Kauffmann et al. (2003) and Kewley et al. (2001), respectively.

As encouraged in Luridiana et al. (2015), we use a cross-converging method to calculate the electron temperatures of O^{++} regions ($T_e([O\,III])$) and electron densities (n_e) with ratios of $[O\,III]\lambda4363/[O\,III]\lambda\lambda4959, 5007$ (Nicholls et al. 2013) and $[S\,II]\lambda6717/[S\,II]\lambda6731$ (Tayal & Zatsarinny 2010). Once the electron temperatures $T_e([O\,III])$ and densities n_e are determined, we can obtain ionic oxygen O^{++} abundances using the $[O\,III]\lambda\lambda4959, 5007/H\beta$ ratios with a relation derived from Izotov et al. (2006). In order to derive the electron temperatures $T_e([O\,II])$ of O^+ regions, we follow an iterative method used in Nicholls et al. (2014),

$$
\begin{aligned}
T_e([O\,II]) = T_e([O\,III]) \\
\times\,(3.0794 - 0.086924Z - 0.1053Z^2 \quad (1) \\
+ 0.010225Z^3),
\end{aligned}
$$

where Z is the total oxygen abundance, $12 + \log(O/H)$. The temperature $T_e([O\,II])$ and abundance Z will converge within five iterations, starting from the O^{++} abundance as the total oxygen abundance. Here, the O^+ abundance is determined from $T_e([O\,II])$ and the $[O\,II]\lambda3727/H\beta$ ratio using the Izotov et al. (2006) relation. Applying other methods from Garnett (1992) or López-Sánchez et al. (2012), we will get an about 0.02

dex higher $T_e([O\,II])$ and an about 0.05 dex lower metallicity for a given $T_e([O\,III])$. Similarly, we will obtain an about 0.03 dex higher $T_e([O\,II])$ and thus arrive at an about 0.05 dex lower metallicity when adopting the standard two-zone temperature model from Izotov et al. (2006) and Andrews & Martini (2013). In our final sample, 31 galaxies also have $[O\,II]\lambda\lambda7320, 7330$ detections above 3σ. Using the $[O\,II]\lambda3727/[O\,II]\lambda\lambda7320, 7330$ ratios to derive $T_e([O\,II])$, we will get lower $T_e([O\,II])$ and higher metallicities. Differences between the corresponding average values of $T_e([O\,II])$ and metallicity are about 360 K and 0.06 dex, respectively.

To estimate the uncertainties in electron temperatures, electron densities and oxygen abundances, we repeat the calculation 2000 times. For every object, we produce a series of fluxes for each emission line with a Gaussian distribution, assuming its average is the measured line flux and standard deviation is the measured error. Then, our final temperature, density and oxygen abundance are deemed to be the median values of these 2000 calculations, and the corresponding errors are estimated as half of the $16\% - 84\%$ range in their distributions. We list the final electron temperatures, electron densities and oxygen abundances associated with our sample in Table 1.

Table 1 The Sample of Metal-poor Galaxies in LAMOST Survey

ID[a]	RA[b] (deg)	DEC[b] (deg)	z[b]	[O II]λ3727	[O III]λ4363	[O III]λ4959	[O III]λ5007	Hα	[S II]λ6717	[S II]λ6731	$I(H\beta)$[c]	$EW(H\beta)$[d] (Å)	$E(B-V)$[e] (mag)	T_e[O III][f] (10^4K)	n_e[f] (cm^{-3})	$12 + \log(O/H)_{T_e}$	$\log(M)$ ($M_\odot$)	$\log(SFR)$ ($M_\odot$ yr^{-1})	SDSS[g]
(1)	(2)	(3)	(4)	(5)	(6)	(7)	(8)	(9)	(10)	(11)	(12)	(13)	(14)	(15)	(16)	(17)	(18)	(19)	(20)
1	0.04352	4.93125	0.031	1.748	0.049	1.760	5.432	2.326	0.114	0.063	1761.90	81.46	0.00	1.16	38.78	8.22	8.250	−0.556	0
				0.054	0.013	0.018	0.051	0.022	0.007	0.007	15.87	0.22	0.01	0.10	42.91	0.12	0.050	0.009	
2	0.22617	18.50614	0.055	2.205	0.030	1.267	3.924	2.135	0.178	0.133	7058.70	46.76	0.00	1.05	99.45	8.29	9.180	0.527	0
				0.018	0.004	0.007	0.019	0.010	0.002	0.001	33.06	0.23	0.01	0.05	15.32	0.06	0.090	0.005	
3	17.64580	2.11408	0.016	2.258	0.032	1.333	3.876	2.685	0.193	0.159	3282.40	34.17	0.00	1.07	234.91	8.28	8.720	−0.782	0
				0.018	0.004	0.004	0.010	0.007	0.002	0.002	8.34	0.31	0.01	0.05	22.81	0.05	0.120	0.003	
4	19.02766	1.03444	0.035	2.164	0.072	1.335	3.977	2.054	0.130	0.108	439.67	43.01	0.00	1.47	272.39	7.88	7.600	−1.185	1
				0.759	0.021	0.022	0.059	0.028	0.007	0.007	5.88	0.26	0.01	0.19	142.65	0.16	0.175	0.014	
5	23.00047	-2.74083	0.018	1.681	0.056	1.632	5.063	2.362	0.177	0.152	797.69	62.08	0.00	1.19	303.92	8.16	7.880	−1.382	0
				0.062	0.010	0.016	0.043	0.021	0.008	0.006	6.63	0.48	0.01	0.08	110.75	0.09	0.180	0.009	
6	31.87386	4.73166	0.011	3.279	0.019	1.089	3.269	2.579	0.267	0.193	5354.90	32.06	0.00	0.97	50.44	8.44	8.230	−0.863	0
				0.026	0.003	0.003	0.007	0.006	0.001	0.001	11.49	0.52	0.01	0.05	8.88	0.07	0.110	0.002	
7	37.72624	1.91723	0.025	3.333	0.069	0.997	2.839	2.860	0.379	0.229	1143.89	12.62	0.20	1.82	30.48	7.67	8.050	−0.931	0
				1.790	0.035	0.031	0.068	0.067	0.017	0.016	26.25	0.58	0.02	0.37	34.73	0.25	0.125	0.024	
8	39.07656	1.75273	0.023	2.130	0.053	1.828	5.206	2.860	0.200	0.144	6174.59	55.21	0.25	1.23	79.89	8.17	8.020	−0.187	0
				0.037	0.009	0.018	0.046	0.026	0.009	0.008	54.01	0.07	0.01	0.06	65.41	0.06	0.015	0.009	
9	43.15004	19.68750	0.029	3.078	0.044	1.270	3.582	1.836	0.174	0.128	4755.70	27.36	0.00	1.22	73.19	8.15	8.010	−0.304	0
				0.015	0.003	0.003	0.008	0.004	0.002	0.002	10.31	0.16	0.01	0.04	21.25	0.04	0.100	0.002	
10	47.66477	5.23287	0.064	2.962	0.015	1.111	3.332	2.853	0.242	0.182	3494.70	35.56	0.00	0.96	113.42	8.44	9.150	0.199	0
				0.053	0.005	0.011	0.029	0.025	0.002	0.002	30.42	0.23	0.01	0.07	15.29	0.10	0.140	0.009	
11	47.91879	2.57282	0.020	1.685	0.098	2.115	6.153	2.582	0.139	0.086	6170.00	103.02	0.00	1.37	15.47	8.05	8.070	−0.389	0
				0.021	0.003	0.005	0.013	0.005	0.001	0.001	12.86	6.06	0.01	0.00	4.26	0.00	0.035	0.002	
12	49.35046	3.50387	0.039	2.179	0.047	1.523	4.753	2.860	0.177	0.129	2297.92	81.85	0.09	1.17	67.05	8.19	8.350	−0.161	0
				0.181	0.009	0.010	0.027	0.016	0.005	0.004	12.85	0.73	0.01	0.08	44.49	0.08	0.140	0.006	
13	51.95898	1.02635	0.109	2.973	0.030	1.111	3.332	2.816	0.443	0.300	1148.30	45.87	0.00	1.11	6.72	8.25	9.020	1.945	1
				1.280	0.232	0.193	0.458	0.403	0.154	0.132	151.78	0.21	0.01	0.06	7.13	0.07	0.395	0.005	
14	123.48118	23.14714	0.015	3.171	0.052	1.245	3.601	2.339	0.226	0.161	1515.70	50.33	0.00	1.33	45.20	8.06	6.600	−1.290	0
				0.077	0.008	0.007	0.017	0.011	0.003	0.003	6.85	0.31	0.01	0.09	29.09	0.08	0.305	0.005	
15	129.35571	37.51241	0.042	2.942	0.050	1.118	3.206	2.639	0.340	0.230	942.03	30.75	0.00	1.34	25.58	8.01	8.550	−0.561	1
				0.178	0.018	0.017	0.038	0.032	0.009	0.009	10.81	0.22	0.01	0.21	26.69	0.18	0.195	0.012	
16	136.71599	41.36413	0.135	3.205	0.056	1.107	3.224	2.166	0.231	0.182	446.71	32.70	0.00	1.43	187.71	7.95	9.270	0.031	1
				0.077	0.016	0.030	0.070	0.045	0.012	0.008	9.18	0.42	0.02	0.17	100.22	0.14	0.280	0.021	
17	139.46461	40.97089	0.024	2.608	0.031	1.403	3.912	2.207	0.262	0.189	721.63	42.77	0.00	1.06	52.69	8.32	8.110	−1.160	0
				0.075	0.013	0.015	0.035	0.020	0.004	0.004	6.30	0.10	0.01	0.14	23.70	0.17	0.095	0.009	
18	139.95418	4.48470	0.012	2.452	0.057	1.376	4.164	2.338	0.227	0.167	2868.10	34.57	0.00	1.32	73.19	8.04	8.070	−1.211	0
				0.194	0.015	0.016	0.041	0.023	0.005	0.004	27.82	0.09	0.01	0.14	38.93	0.13	0.180	0.010	
19	140.17699	5.73677	0.038	1.029	0.082	2.450	7.272	2.860	0.100	0.071	11516.86	96.12	0.23	1.20	38.78	8.22	8.220	0.525	0
				0.014	0.003	0.007	0.019	0.008	0.001	0.001	30.64	0.31	0.01	0.02	23.27	0.02	0.205	0.003	
20	140.92796	3.36689	0.012	2.760	0.050	1.340	3.788	2.312	0.210	0.150	1090.50	34.17	0.00	1.30	52.69	8.07	7.330	−1.629	1
				0.086	0.014	0.015	0.035	0.021	0.006	0.005	9.79	0.16	0.01	0.14	41.58	0.12	0.355	0.010	
21	142.63454	34.43079	0.017	1.689	0.045	1.443	4.180	2.860	0.190	0.104	1297.69	34.84	0.01	1.10	56.29	8.24	7.740	−1.114	1
				0.037	0.010	0.012	0.029	0.020	0.006	0.006	8.78	0.21	0.01	0.10	66.58	0.11	0.300	0.007	
22	145.71992	35.79055	0.015	1.676	0.055	1.538	4.217	2.210	0.166	0.081	2180.30	100.80	0.00	1.21	19.54	8.10	7.339	−1.147	1
				0.021	0.005	0.006	0.015	0.008	0.002	0.002	7.31	0.15	0.01	0.03	10.87	0.03	0.074	0.004	
23	146.00691	50.87919	0.038	2.683	0.028	1.048	2.923	2.471	0.320	0.235	1322.90	37.23	0.00	1.12	73.19	8.19	8.960	−0.485	1
				0.036	0.009	0.008	0.018	0.015	0.004	0.003	7.63	0.64	0.01	0.11	22.38	0.13	0.185	0.006	
24	147.03999	2.52892	0.021	2.681	0.032	1.348	4.014	2.844	0.279	0.194	2646.10	35.59	0.00	1.18	30.48	8.19	8.270	−0.638	1
				0.086	0.009	0.010	0.026	0.019	0.005	0.006	16.94	0.09	0.01	0.10	26.41	0.10	0.175	0.007	
25	148.70041	38.45017	0.017	3.040	0.024	0.939	2.683	2.440	0.370	0.269	1971.30	29.46	0.00	1.09	62.79	8.24	8.320	−1.003	1
				0.036	0.008	0.008	0.016	0.014	0.004	0.004	11.02	0.17	0.01	0.13	17.34	0.15	0.070	0.006	
26	154.10216	37.91277	0.004	0.687	0.097	1.346	4.106	2.860	0.074	0.056	3778.46	138.04	0.01	1.64	115.85	7.63	6.550	−2.029	1

Table 1 — *Continued.*

IDa	RAb (deg)	DECb (deg)	zb	$I(\lambda)/I(H\beta)$ c							$I(H\beta)$c	$EW(H\beta)$d (Å)	$E(B-V)$e (mag)	T_e[O III]f (10^4K)	n_e^f (cm^{-3})	$12 + \log(O/H)_{Te}$	$\log(M)$ ($M_\odot$)	$\log$ (SFR) ($M_\odot$ yr^{-1})	SDSSg
				[O II]λ3727	[O III]λ4363	[O III]λ4959	[O III]λ5007	Hα	[S II]λ6717	[S II]λ6731									
(1)	(2)	(3)	(4)	(5)	(6)	(7)	(8)	(9)	(10)	(11)	(12)	(13)	(14)	(15)	(16)	(17)	(18)	(19)	(20)
				0.022	0.003	0.003	0.007	0.005	0.001	0.002	6.15	0.19	0.01	0.02	52.03	0.01	0.070	0.002	
27	157.45534	16.18091	0.011	3.230	0.040	1.187	3.468	2.007	0.278	0.203	1701.80	27.67	0.00	1.22	64.22	8.16	8.430	−1.548	1
				0.059	0.010	0.012	0.028	0.016	0.005	0.005	13.14	0.21	0.01	0.11	33.81	0.11	0.005	0.008	
28	161.47824	1.06829	0.026	2.243	0.045	1.549	4.167	2.860	0.216	0.161	22426.28	108.84	0.18	1.17	91.11	8.19	7.860	0.478	1
				0.012	0.002	0.003	0.006	0.004	0.001	0.001	33.64	0.24	0.01	0.02	7.99	0.02	0.005	0.001	
29	162.63853	22.31531	0.046	2.084	0.052	1.394	3.964	2.826	0.313	0.218	1269.00	39.66	0.00	1.25	16.87	8.07	8.360	−0.308	1
				0.030	0.007	0.008	0.019	0.014	0.004	0.004	6.06	0.19	0.01	0.06	15.18	0.06	0.305	0.005	
30	163.09535	32.63737	0.005	2.665	0.028	1.020	2.611	2.412	0.319	0.225	1828.20	20.58	0.00	1.18	22.43	8.12	7.640	−2.135	1
				0.022	0.004	0.004	0.007	0.006	0.002	0.001	4.74	0.06	0.01	0.06	8.89	0.06	0.110	0.002	
31	170.34760	6.66713	0.009	2.816	0.064	1.052	3.069	2.860	0.257	0.193	1169.43	27.91	0.01	1.30	99.45	8.03	7.410	−1.762	1
				0.073	0.013	0.012	0.027	0.025	0.006	0.006	9.96	0.05	0.01	0.15	51.12	0.14	0.280	0.009	
32	186.62852	28.84698	0.027	3.039	0.046	0.929	2.844	2.860	0.423	0.315	1498.23	25.58	0.03	1.44	89.21	7.91	8.650	−0.727	0
				0.062	0.012	0.011	0.025	0.024	0.007	0.006	12.52	0.35	0.01	0.15	32.31	0.12	0.075	0.009	
33	187.70251	12.04523	0.004	1.118	0.109	1.565	4.442	2.697	0.109	0.080	4437.80	85.03	0.00	1.67	73.19	7.70	6.390	−1.976	1
				0.016	0.002	0.003	0.008	0.005	0.001	0.001	7.57	0.16	0.01	0.02	26.96	0.01	0.070	0.002	
34	188.68443	10.71915	0.032	2.124	0.052	1.531	4.283	2.740	0.185	0.171	1392.00	67.30	0.00	1.23	464.63	8.13	8.240	−0.583	1
				0.017	0.004	0.005	0.012	0.008	0.002	0.002	3.93	0.43	0.01	0.04	34.42	0.04	0.020	0.003	
35	189.23994	10.13030	0.027	1.485	0.039	1.366	4.083	2.856	0.249	0.183	445.10	37.11	0.00	1.13	85.32	8.14	8.640	−1.205	1
				0.064	0.016	0.019	0.049	0.034	0.008	0.008	5.16	0.31	0.01	0.17	62.00	0.19	0.225	0.012	
36	189.52870	10.16557	0.004	0.642	0.099	1.953	5.567	2.703	0.089	0.062	2579.20	156.19	0.00	1.43	16.87	7.90	6.590	−2.177	1
				0.019	0.003	0.004	0.011	0.006	0.001	0.001	5.14	0.05	0.01	0.02	15.98	0.01	0.035	0.002	
37	189.73721	38.09029	0.007	2.820	0.032	1.046	2.960	2.729	0.367	0.257	1454.40	11.09	0.00	1.19	20.55	8.13	8.320	−1.887	1
				0.040	0.007	0.007	0.014	0.013	0.004	0.004	6.43	0.23	0.01	0.09	15.20	0.09	0.060	0.005	
38	196.86958	54.44713	0.033	2.544	0.035	1.524	4.133	2.860	0.242	0.190	10397.45	73.00	0.03	1.08	162.86	8.30	8.590	0.381	1
				0.014	0.003	0.004	0.009	0.006	0.001	0.001	22.36	0.13	0.01	0.03	9.56	0.03	0.075	0.002	
39	198.22404	17.20867	0.052	2.129	0.049	1.436	4.157	2.860	0.210	0.150	3750.41	70.01	0.21	1.21	57.52	8.12	8.020	0.285	1
				0.071	0.014	0.016	0.039	0.027	0.005	0.006	34.19	0.11	0.01	0.13	44.45	0.14	0.155	0.009	
40	212.67758	38.71842	0.025	3.061	0.028	1.114	3.227	2.860	0.378	0.274	1216.35	23.52	0.00	1.09	52.69	8.27	8.370	−0.796	1
				0.041	0.008	0.008	0.019	0.017	0.005	0.004	6.84	0.26	0.01	0.10	22.31	0.12	0.160	0.006	
41	220.85265	28.30123	0.013	2.490	0.029	1.199	3.575	2.551	0.291	0.206	2186.30	34.68	0.00	1.07	27.92	8.28	8.210	−1.161	0
				0.038	0.007	0.007	0.018	0.013	0.003	0.003	10.51	0.67	0.01	0.09	16.76	0.11	0.120	0.005	
42	222.59503	11.40265	0.006	1.260	0.036	1.543	4.234	1.543	0.115	0.214	2445.60	68.75	0.00	1.10	475.04	8.39	7.500	−1.823	0
				12.190	0.007	0.008	0.019	0.007	0.003	0.002	10.98	0.37	0.01	0.07	48.24	0.25	0.080	0.005	
43	321.52011	8.68640	0.010	1.850	0.061	1.617	4.840	2.809	0.200	0.144	2200.90	49.17	0.00	1.24	44.22	8.12	7.900	−1.386	0
				0.030	0.007	0.009	0.023	0.014	0.002	0.002	10.48	0.21	0.01	0.06	22.79	0.06	0.100	0.005	
44	325.30099	8.68733	0.032	3.758	0.033	1.055	3.104	2.678	0.343	0.248	1105.70	23.31	0.00	1.19	55.05	8.20	8.600	−0.675	0
				0.032	0.007	0.006	0.016	0.012	0.003	0.003	4.89	0.34	0.01	0.09	15.64	0.09	0.325	0.004	
45	327.59015	7.60371	0.027	1.501	0.094	1.929	5.831	2.420	0.109	0.082	1003.90	75.16	0.00	1.37	116.11	8.02	8.030	−0.952	0
				0.098	0.009	0.012	0.033	0.014	0.003	0.004	5.56	0.24	0.01	0.05	72.01	0.04	0.130	0.006	
46	336.10513	6.25363	0.016	2.475	0.054	1.631	4.790	2.327	0.156	0.130	2647.40	63.85	0.00	1.20	260.72	8.19	8.200	−0.962	0
				0.010	0.007	0.008	0.020	0.010	0.003	0.003	10.75	0.34	0.01	0.05	53.29	0.05	0.160	0.004	
47	341.07831	5.36256	0.006	2.681	0.046	1.436	4.053	2.669	0.228	0.177	6841.20	55.27	0.00	1.19	154.47	8.18	7.960	−1.344	0
				0.022	0.003	0.003	0.007	0.005	0.001	0.001	11.57	0.46	0.01	0.02	10.14	0.02	0.190	0.002	
48	352.58768	5.52682	0.014	2.313	0.057	1.646	4.242	2.860	0.234	0.173	13399.27	66.73	0.10	1.26	79.89	8.10	7.800	−0.306	0
				0.018	0.003	0.003	0.007	0.005	0.001	0.002	21.79	0.29	0.01	0.02	14.80	0.02	0.010	0.002	

Notes: — Basic information, emission line fluxes, electron temperatures and oxygen abundances for our sample galaxies. For every object, the first (second) line presents the parameter (error) values. [a] 'ID' is the serial number for every object and it will be referred to throughout this paper. [b] The right ascension (J2000) and declination (J2000) of our sample galaxies are given in units of degrees. The RA, DEC, and redshift are obtained from the header of the spectral FITS files. [c] Reddening corrected emission line fluxes for our sample galaxies measured from the LAMOST spectra are relative to $H\beta$. The $H\beta$ fluxes are reported in units of 10^{-17} erg s^{-1} cm^{-2}. [d] The $H\beta$ equivalent widths are given in units of Å, assuming the mean values of observed flux intensities within 50 Å wide component around the $H\beta$ as the continuum spectral flux intensities. [e] The nebular color excesses are derived from the observed flux ratios $H\alpha/H\beta$, and are assumed to be zero when the observed flux ratios $H\alpha/H\beta$ are less than 2.86. [f] Electron temperatures are computed from the oxygen emission line ratios [O III]λλ4959, 5007/[O III]λ4363. Electron densities are calculated from an iterative process with [O III]λλ4959, 5007/[O III]λ4363 and [S II]λ6717/[S II]λ6731 ratios. [g] The flag numbers indicate the spectral detected states for our objects with SDSS. "1" ("0") represent this object has (not) been spectroscopically detected by SDSS.

Figure 4 shows the distributions of color excesses, electron densities, electron temperatures and oxygen abundances. The electron densities and temperatures in our sample range from 6.7 to $475.0\,\mathrm{cm}^{-3}$ and $(0.96-1.82) \times 10^4\,\mathrm{K}$, with median values of $67.0\,\mathrm{cm}^{-3}$ and $1.21 \times 10^4\,\mathrm{K}$, respectively. Their oxygen abundances range from 7.63 to 8.46, with a median of 8.16. The only XMPG found in our sample is ID26 with $12 + \log(\mathrm{O/H}) = 7.63 \pm 0.01$, which has already been found by Izotov et al. (2012a) with $12 + \log(\mathrm{O/H}) = 7.64 \pm 0.01$. Interestingly, galaxy ID33, also named RC2 A1228+12, was regarded as an XMPG in Kunth & Östlin (2000) and Brorby et al. (2014), but the metallicity $12 + \log(\mathrm{O/H}) = 7.70 \pm 0.01$ indicates it is not an XMPG. This judgement was also supported by Pustilnik et al. (2002) and Izotov et al. (2012b) with metallicity measurements of 7.73 ± 0.06 and 7.70 ± 0.01, respectively.

4 STELLAR MASSES AND STAR FORMATION RATES

4.1 Stellar Masses

To determine the galactic stellar masses of our sample galaxies, we use the IDL code library FAST developed by Kriek et al. (2009) to perform spectral energy distribution (SED) fitting. FAST compares photometry measurements with stellar population synthesis models, based on a minimum χ^2 template-fitting procedure, to determine mass-to-light ratios, which can be used to estimate the stellar masses of galaxies. We use the stellar templates of Bruzual & Charlot (2003) and a Chabrier (2003) initial mass function (IMF) to synthesize magnitudes. These models span four metallicities (0.004, 0.008, 0.02, 0.05 $Z_\odot$) and an exponentially decreasing star formation model (SFR $\propto \mathrm{e}^{-\mathrm{t}/\tau}$) with a step of $\Delta \log(\tau) = 0.1$ from $6.6 \leq \log(\tau) \leq 10.8$. We assume the dust attenuation law from Calzetti et al. (2000) allowing $E(B - V)$ to vary from 0.0 to 2.0 and stellar population ages ranging from 0 to 100 Gyr. To determine the uncertainties of stellar masses, we use Monte Carlo simulations and define the number of simulations as 1000. We choose the confidence interval as 68%.

Photometric measurements are collected from various survey catalogs. We adopt values of MODELMAG magnitudes of u, g, r, i and z bands from SDSS DR12 photometry catalog (Abazajian et al. 2004; Alam et al. 2015), magnitudes of J, H and K_s bands from 2MASS All-Sky Point Source Catalog and 2MASS All-Sky Extended Source Catalog (Skrutskie et al. 2006), magnitudes of $W1$ (3.4 μm) and $W2$ (4.6 μm) from the All

WISE Source Catalog (Wright et al. 2010), and magnitudes of far ultraviolet (FUV) and near ultraviolet from *GALEX* GR6/7 Data Release Catalog (Bianchi et al. 2014). However, not all of our sample galaxies have these photometric measurements. For example, 45 galaxies have FUV photometry, but three galaxies are not located in areas surveyed by *GALEX*. For these three galaxies, we just use their magnitudes from the u band to the $W2$ band to perform SED fitting. We find our sample galaxies span three orders with $6.39 \leq \log(M/M_\odot) \leq 9.27$. We should note that we do not make the point spread function match our photometric data using the same observation aperture, which may lead to some uncertainties in stellar mass measurements. The average and median values of stellar mass measurement uncertainties are 0.14 dex and 0.12 dex, respectively. However, comparing our results with total stellar masses in the MPA-JHU catalog (Kauffmann et al. 2003; Brinchmann et al. 2004) for galaxies included in the MPA-JHU catalog, we find differences in average and median values are about 0.1 dex and 0.03 dex, respectively.

4.2 Star Formation Rates

In this work, we use the Hα emission line luminosities to determine dust-corrected SFRs, assuming a Chabrier (2003) IMF and solar metallicity. The SFR can be calculated from Hα luminosity as

$$\mathrm{SFR}(M_\odot\ \mathrm{yr}^{-1}) = R \times L(\mathrm{erg\ s}^{-1}), \qquad (2)$$

where $R = 4.4 \times 10^{-42}$. However, the latest work of Ly et al. (2016a) demonstrated that the above parameter R would overestimate the SFR at lower metallicities, and gave the metallicity-dependent parameter R as

$$\begin{aligned}
\log(R) &= \log\left(\frac{\mathrm{SFR}}{L(\mathrm{H}\alpha)}\right) \\
&= -41.34 + 0.39y + 0.127y^2, \qquad (3)
\end{aligned}$$

where $y = \log(\mathrm{O/H}) + 3.31$. The final stellar masses and SFRs in our sample are listed in Table 1.

5 THE MASS–METALLICITY AND MASS–METALLICITY–SFR RELATIONS

5.1 The Mass–Metallicity Relation

In panel (a) of Figure 5, we plot the MZR with T_e-based metallicities for our sample. These dot symbols representing our galaxies are color-coded by their SFRs. For comparison, we also show the MZRs obtained by Andrews & Martini (2013) and Berg et al. (2012) for their galaxy sample in the local universe, which are
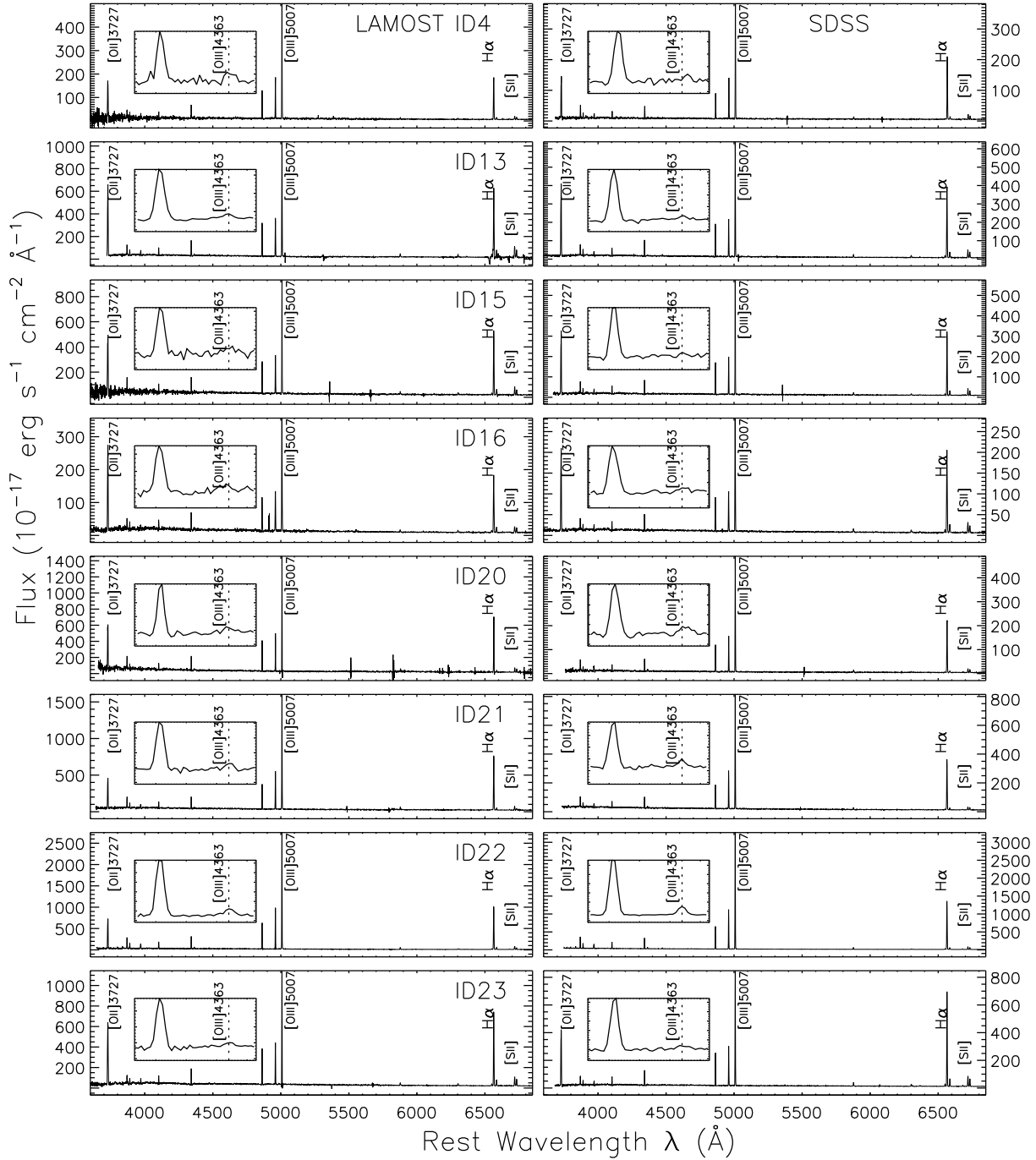
Fig. 3 Example spectra of objects in our sample that have been spectrally detected with both LAMOST and SDSS. For every object, the *left panel* shows its LAMOST spectrum, while the *right panel* shows its SDSS spectrum. *Inserted panels* show magnified in spectra adjacent to the [O III]λ4363 lines.

shown as solid and dot-dashed black lines, based on T_e metallicity calculation.

The MZR in Berg et al. (2012) is a simple linear fit for a small sample of low luminosity metal-poor galaxies with stellar masses $\log(M/M_\odot)$ ranging from 5.9 to 9.15. As shown in panel (a), the metallicities of

our metal-poor galaxies are systematically higher than the MZR in Berg et al. (2012) by about 0.25 dex. The MZR of Andrews & Martini (2013) is fitted with an asymptotic logarithmic formula for about two hundred thousand nearby star forming galaxies with stellar mass from $\log(M/M_\odot) = 7.4 - 10.5$. Most of our galax-
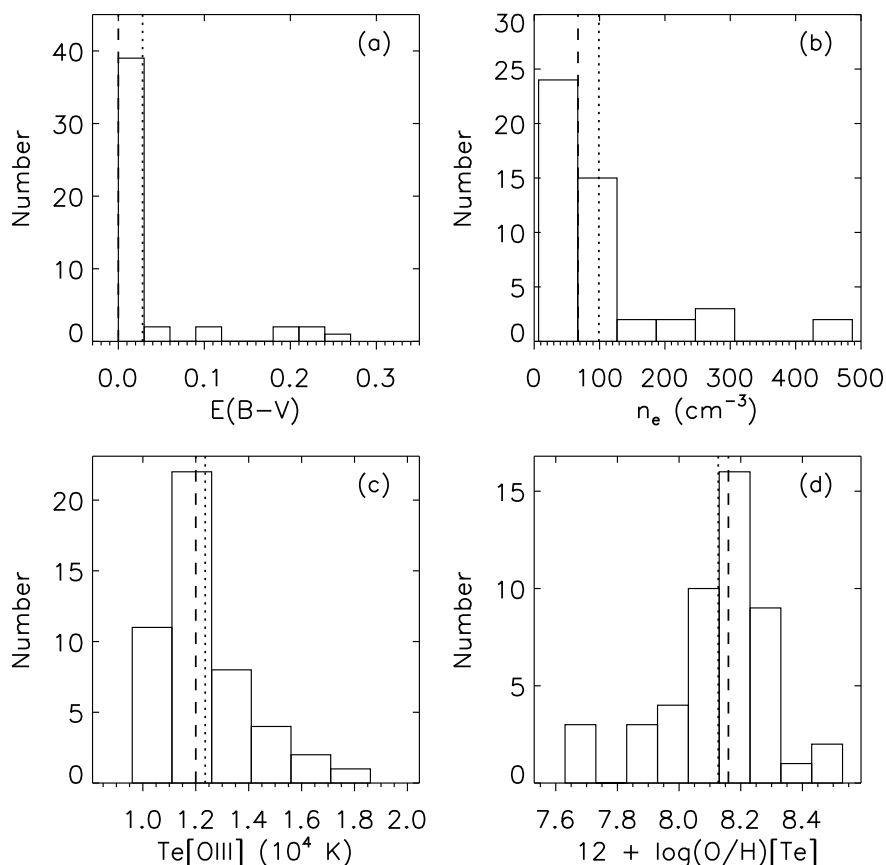
Fig. 4 The distributions of color excesses, electron densities, electron temperatures and oxygen abundances for our sample galaxies. The *dashed lines* represent median values of these parameters, 0.00 mag, 67.0 cm^{-3}, 1.20×10^4 K and 8.16, respectively. The *dotted lines* represent the average values of 0.03 mag, 98.9 cm^{-3}, 1.24×10^4 K and 8.13, respectively.

ies are in good agreement with the MZR in Andrews & Martini (2013). The average and median values of residuals between metallicities and MZR are 0.0015 dex and 0.025 dex, respectively. We find that the scatter in the MZR from LAMOST data, relative to the MZR of Andrews & Martini (2013), is 0.28 dex.

5.2 Mass–Metallicity–SFR Relation

The mass–metallicity–SFR relation, also referred to as the fundamental metallicity relation (FMR), is proposed by Mannucci et al. (2010) to describe the anti-correlation between metallicity and SFR at fixed stellar mass. Mannucci et al. (2010) defined a new quantity $\mu_\alpha = \log(M) - \alpha \log(\mathrm{SFR})$ to minimize the dispersion in MZR for local galaxies. Using the semi-empirical "strong-line" metallicity calibration of Maiolino et al. (2008), Mannucci et al. (2010) yielded $\alpha = 0.32$. However, Andrews & Martini (2013) found a new value of $\alpha = 0.66$ based on the T_e metallicity calculation method. In this work, we assume the value of $\alpha = 0.66$,

since metallicities in our sample galaxy are also determined with the T_e method.

Panel (b) of Figure 5 shows the FMR for our metal-poor galaxies. The solid black line represents the FMR derived by Andrews & Martini (2013). Most of our galaxies are consistent with the FMR; the average and median values of the residuals between metallicities and FMR are 0.002 dex and 0.009 dex, respectively. The scatter in the FMR from LAMOST data, relative to the FMR of Andrews & Martini (2013), is about 0.24 dex.

6 DISCUSSION

6.1 Comparison with SDSS Spectrum

Among our metal-poor galaxy sample, 24 galaxies are also spectrally detected by SDSS, and are marked with flag "1" in the 'SDSS' column of Table 1. We select these galaxies from SDSS DR12 by matching the RA and DEC with our sample within one arcsec. We also obtain the emission line fluxes from these 24 SDSS galaxy spectra and find that there are 19 spectra with [O III]$\lambda4363$ detec-
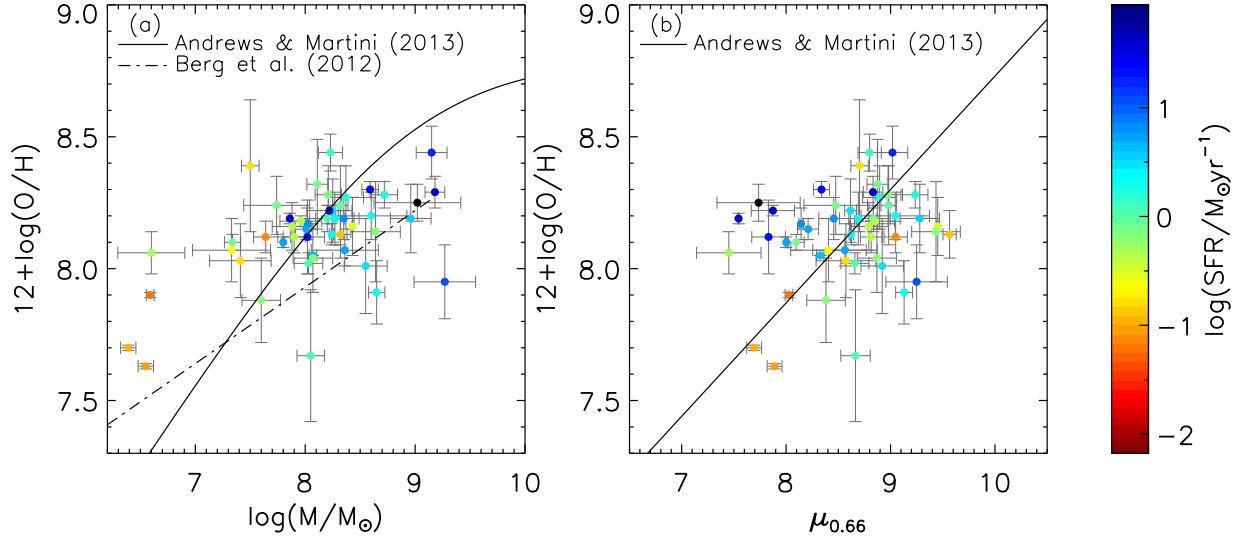
Fig. 5 The T_e method mass–metallicity relation and fundamental metallicity relation for our sample galaxies. In both panels, dot symbols representing our galaxies are color-coded by their SFRs. Panel (a): the solid and dot-dashed black lines represent MZRs derived from nearby star forming galaxies by Andrews & Martini (2013) and Berg et al. (2012), respectively. Panel (b): the solid black line represents the FMR relation derived by Andrews & Martini (2013), who assumed the coefficient on $\log(\text{SFR})$ is 0.66 with $\mu_{0.66} = \log(M) - 0.66 \log(\text{SFR})$. The uncertainties in stellar masses are presented with 68% confidence interval limits.
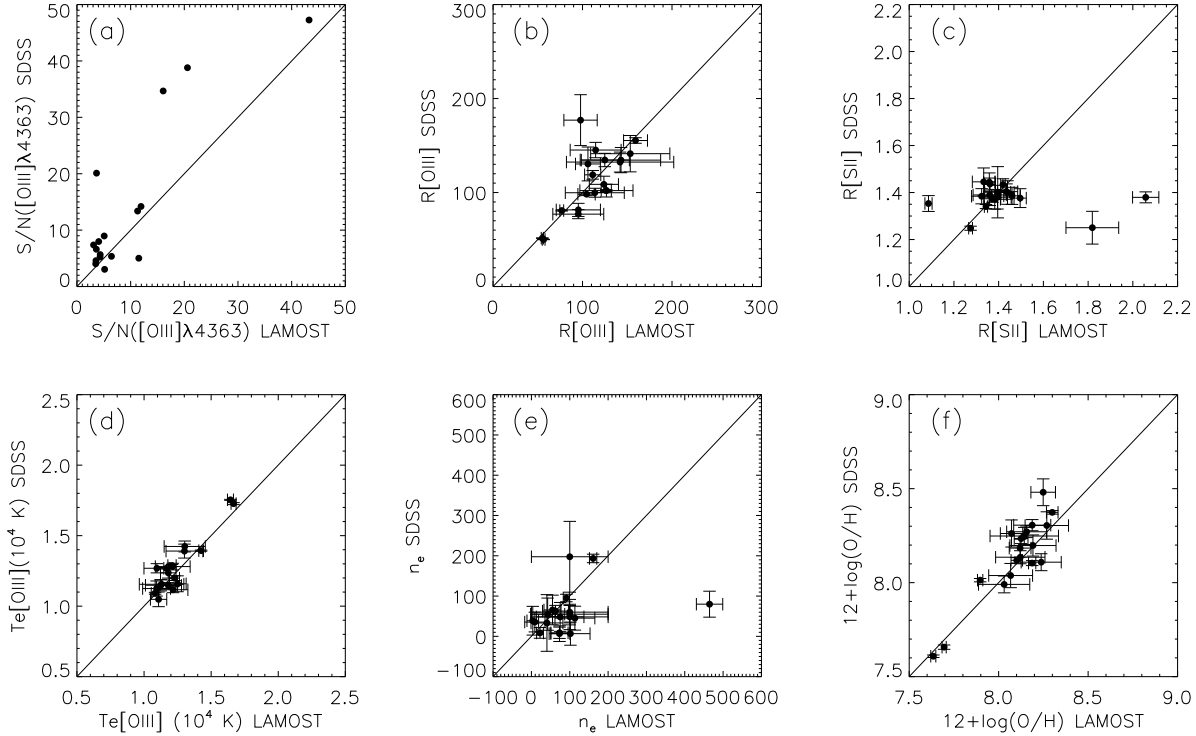
Fig. 6 Comparisons of S/N values for weak [O III]λ4363 lines, [O III] line flux ratios (R[O III] = [O III]$\lambda\lambda$4959, 5007/[O III]λ4363), [S II] line flux ratios (R[S II] = [S II]λ6717/[S II]λ6731), electron temperatures, electron densities and oxygen abundances derived from LAMOST spectra and from SDSS spectra for 19 galaxies in our sample. The *solid lines* indicate equality between the LAMOST and SDSS measurements.

tions above 3σ. Similarly, we calculate their metallicities with the T_e method.

Figure 6 shows comparisons of S/Ns for weak [O III]$\lambda4363$ lines, [O III] and [S II] line fluxes ratios ([O III]$\lambda\lambda4959$, 5007/[O III]$\lambda4363$, [S II]$\lambda6717$/[S II]$\lambda6731$), electron temperatures (T_e([O III])), electron densities (n_e) and oxygen abundances derived from LAMOST spectra and from SDSS spectra. The quality of SDSS spectra is generally better than that from LAMOST with higher S/N on the weak [O III]$\lambda4363$. Panels (b) and (d) display strong correlation for [O III] ratios and electron temperatures between the LAMOST and SDSS measurements. Although there are several objects that have large dispersion in the comparison that considers [S II] ratios and electron densities, the differences between the final oxygen abundances from these two measurements are less than 0.01 dex.

6.2 Comparison with Other [O III]$\lambda4363$ Galaxy Samples

All of the galaxies in our sample are selected from the local universe ($0.004 \leq z \leq 0.14$), and have stellar masses spanning three orders with $6.39 \leq \log(M/M_\odot) \leq 9.27$. The only XMPG is detected with $12 + \log(\mathrm{O/H}) = 7.63 \pm 0.01$ in our sample, however, it has already been found by Izotov et al. (2012a). In previous decades, there have been many efforts to search for [O III]$\lambda4363$ galaxies and XMPGs in the local universe. For example, Kniazev et al. (2003) discovered 12 XMPGs with $7.13 \leq 12 + \log(\mathrm{O/H}) \leq 7.64$ using SDSS spectroscopy. Izotov et al. (2006) found six new XMPGs in 310 [O III]$\lambda4363$ galaxies from SDSS DR3. Berg et al. (2012) also investigated 19 [O III]$\lambda4363$ low luminosity galaxies with the MMT telescope. Additionally, for the intermediate and high redshift universe, Kakazu et al. (2007) mapped 12 XMPGs to $z = 1.0$ with DEIMOS on Keck II. Ly et al. (2014) identified four XMPGs in 20 emission-line galaxies with [O III]$\lambda4363$ at $z = 0.065 - 0.90$ by the MMT and Keck telescopes. Amorín et al. (2014) also discovered four XMPGs from 31 low-luminosity extreme emission line galaxies out to $z = 0.9$ in the VIMOS Ultra-Deep Survey. Recently, Ly et al. (2015) found 28 metal-poor galaxies with stellar mass spanning $7.1 \times 10^7 - 2.2 \times 10^9\,M_\odot$ in DEEP2 at redshift $z \sim 0.8$. Ly et al. (2016a) also presented a larger sample of 164 galaxies with a weak [O III]$\lambda4363$ line at $z = 0.1-$ -1.0 from the "Metal Abundances across Cosmic Time" survey. Compared with these samples, the number of galaxies in our sample is small, which may be caused

by selection from a limiting magnitude of LAMOST. However, the fraction of galaxies with [O III]$\lambda4363$ detections in LAMOST data is nearly the same as that in SDSS.

6.3 MZR and FMR

The MZR, which was originally established by Lequeux et al. (1979) and developed by Garnett & Shields (1987), Skillman et al. (1989), Brodie & Huchra (1991), Zaritsky et al. (1994), Tremonti et al. (2004), indicates that the metallicities of galaxies correlate with their stellar masses. Taking SFR into consideration, Mannucci et al. (2010) found that metallicity decreases with increasing SFR at low stellar mass, but does not depend on SFR at high stellar mass ($\log(M/M_\odot) \geq 10.7$). However, Yates et al. (2012) suggested that high-mass ($\log(M/M_\odot) \geq 10.4$) galaxies have lower metallicities when their SFRs are lower. These different results may be caused by different metallicity calculation methods. In addition, the MZR is also affected by other physical parameters, such as stellar age and gas fraction. Lian et al. (2015) found that metallicity is strongly dependent on $D_n(4000)$, who interpreted galaxies with older stellar ages as having higher metallicities at a fixed stellar mass. Hughes et al. (2013) found that galaxies with higher gas fraction have lower metallicities at a fixed mass. Lara-López et al. (2010) and Mannucci et al. (2010) argued that the MZR is in fact a projection of FMR. In past years, many efforts (e.g., Mannucci et al. (2010); Berg et al. (2012); Andrews & Martini (2013); Salim et al. (2014); Ly et al. (2015, 2016b)) have been made to explore the relationship between MZR and FMR from low mass to high mass, as well as the evolution with redshift. In the local universe, metallicity increases with increasing stellar mass, and decreases with increasing SFR at a fixed stellar mass when $\log(M/M_\odot) \leq 10.5$. Salim et al. (2014) found that metallicity is anti-corrected with specific SFR regardless of different metallicity indicators or methods used when $9.0 \leq \log(M/M_\odot) \leq 10.5$, but the dependence is weak or absent for massive galaxies when $\log(M/M_\odot) > 10.5$. Salim et al. (2014) also demonstrated that the relative specific SFR is a more physically motivated second parameter for the MZR, and found that the overall scatter in the FMR does not significantly decrease relative to the dispersion in the MZR. Recently, Bothwell et al. (2016) reported that the FMR is between stellar mass, metallicity and gas mass instead of the SFR. In addition, Kashino et al. (2016) measured the metallicity of star forming galaxies based on Dopita et al. (2016) and Maiolino et al. (2008) calibrations, and found that

whether the FMR exists or not depends on the metallicity measurement method. The dependence on metallicity and SFR at high stellar mass is still under debate (Kashino et al. 2016). For the intermediate redshift universe, Ly et al. (2016b) clearly showed that the MZR evolves toward lower metallicity at fixed stellar mass with increasing redshift z, and found a much weaker dependence of MZR on SFR than in the local universe.

In panel (a) of Figure 5, we color-code our galaxy points with their SFRs. Figure 5 shows that most of the galaxies in our sample have higher metallicities than the galaxies in Berg et al. (2012), but are consistent with the result in Andrews & Martini (2013). The difference between our work and Berg et al. (2012) may be caused by the difference in sample selection and calibrations for electron temperatures $T_e([O\,III])$ and $T_e([O\,II])$. Andrews & Martini (2013) found that the scatter in MZR for the M-SFR stacks, in which every point represents the mean value of metallicity for galaxies in the same stellar-mass bin and same SFR bin, is 0.22 dex, while the scatter in the FMR is 0.13 dex. The decrease of scatter value in Andrews & Martini (2013) reflects a strong SFR-dependence on the MZR. From visual examination, we do not find strong dependence of MZR on SFR. However, the scatter in FMR is 0.24 dex, lower than the 0.28 dex scatter in MZR, suggesting MZR is weakly dependent on SFR. We note that the average and median values of metallicity measurement uncertainties are 0.09 dex and 0.08 dex, respectively. The average and median values of stellar mass measurement uncertainties are about 0.14 dex and 0.12 dex, respectively. The larger scatters in MZR and FMR compared with Andrews & Martini (2013) relations may be caused by the small galaxy sample size, as well as the measurement uncertainties on stellar mass.

7 SUMMARY

We inspect all 92 510 galaxies in LAMOST DR3 and DR4 Q1 and Q2, and select 48 galaxies with $[O\,III]\lambda4363$ detected at $\geq 3\sigma$ as our metal-poor galaxy sample. Using the T_e method, we obtain the metallicities of these metal-poor galaxies with a median of $12 + \log(O/H) = 8.16$, spanning the range from 7.63 to 8.46. The most metal-deficient galaxy in our sample is ID26 with $12 + \log(O/H) = 7.63\pm0.01$, which is the only XMPG we found, but it has already been discovered by Izotov et al. (2012a). We also confirm that the galaxy ID33 (RC2 A1228+12) is not an XMPG.

With multiband photometric data from FUV to NIR and Hα measurements, we determine the stellar masses and dust-corrected SFRs, based on the SED fitting and reddening corrected Hα luminosities, respectively. We compare the relationship between stellar mass, T_e-based metallicity and SFR of our galaxies with galaxies in the local universe. We find that the metallicities of our galaxies are in good agreement with the local T_e-based MZR in Andrews & Martini (2013) with average and median values of residuals 0.0015 dex and 0.025 dex, respectively. However, the MZR in Berg et al. (2012) may be systematically lower than the metallicities of our metal-poor galaxies. Assuming the coefficient of $\alpha = 0.66$, we find most of our galaxies are consistent with the FMR in Andrews & Martini (2013). However, the scatter in FMR is 0.24 dex, lower than the 0.28 dex scatter in MZR, suggesting MZR has a weak dependence on SFR.

References

Abazajian, K., Adelman-McCarthy, J. K., Agüeros, M. A., et al. 2004, AJ, 128, 502

Alam, S., Albareti, F. D., Allende Prieto, C., et al. 2015, ApJS, 219, 12

Allende Prieto, C., Lambert, D. L., & Asplund, M. 2001, ApJ, 556, L63

Aller, L. H., ed. 1984, Astrophysics and Space Science Library, 112, Physics of Thermal Gaseous Nebulae

Amorín, R., Sommariva, V., Castellano, M., et al. 2014, A&A, 568, L8

Andrews, B. H., & Martini, P. 2013, ApJ, 765, 140

Baldwin, A., Phillips, M. M., & Terlevich, R. 1981, PASP, 93, 817

Berg, D. A., Skillman, E. D., Marble, A. R., et al. 2012, ApJ, 754, 98

Bianchi, L., Conti, A., & Shiao, B. 2014, Advances in Space Research, 53, 900

Bothwell, M. S., Maiolino, R., Peng, Y., et al. 2016, MNRAS, 455, 1156

Brinchmann, J., Charlot, S., White, S. D. M., et al. 2004, MNRAS, 351, 1151

Brodie, J. P., & Huchra, J. P. 1991, ApJ, 379, 157

Brorby, M., Kaaret, P., & Prestwich, A. 2014, MNRAS, 441, 2346

Bruzual, G., & Charlot, S. 2003, MNRAS, 344, 1000

Calzetti, D., Armus, L., Bohlin, R. C., et al. 2000, ApJ, 533, 682

Chabrier, G. 2003, PASP, 115, 763

Cid Fernandes, R., Mateus, A., Sodré, L., Stasińska, G., & Gomes, J. M. 2005, MNRAS, 358, 363

Cui, X.-Q., Zhao, Y.-H., Chu, Y.-Q., et al. 2012, RAA (Research in Astronomy and Astrophysics), 12, 1197

Dopita, M. A., Kewley, L. J., Sutherland, R. S., & Nicholls, D. C. 2016, Ap&SS, 361, 61

Doyle, M. T., Drinkwater, M. J., Rohde, D. J., et al. 2005, MNRAS, 361, 34

Froese Fischer, C., & Tachiev, G. 2004, Atomic Data and Nuclear Data Tables, 87, 1

Garnett, D. R. 1992, AJ, 103, 1330

Garnett, D. R., & Shields, G. A. 1987, ApJ, 317, 82

Hu, N., Su, S.-S., & Kong, X. 2016, RAA (Research in Astronomy and Astrophysics), 16, 42

Hughes, T. M., Cortese, L., Boselli, A., Gavazzi, G., & Davies, J. I. 2013, A&A, 550, A115

Hummer, D. G., & Storey, P. J. 1987, MNRAS, 224, 801

Izotov, Y. I., Stasińska, G., Meynet, G., Guseva, N. G., & Thuan, T. X. 2006, A&A, 448, 955

Izotov, Y. I., & Thuan, T. X. 2004, ApJ, 616, 768

Izotov, Y. I., Thuan, T. X., & Guseva, N. G. 2012a, A&A, 546, A122

Izotov, Y. I., Thuan, T. X., & Privon, G. 2012b, MNRAS, 427, 1229

Kakazu, Y., Cowie, L. L., & Hu, E. M. 2007, ApJ, 668, 853

Kashino, D., Renzini, A., Silverman, J. D., & Daddi, E. 2016, ApJ, 823, L24

Kauffmann, G., Heckman, T. M., White, S. D. M., et al. 2003, MNRAS, 341, 33

Kewley, L. J., Dopita, M. A., Sutherland, R. S., Heisler, C. A., & Trevena, J. 2001, ApJ, 556, 121

Kisielius, R., Storey, P. J., Ferland, G. J., & Keenan, F. P. 2009, MNRAS, 397, 903

Kniazev, A. Y., Grebel, E. K., Hao, L., et al. 2003, ApJ, 593, L73

Kriek, M., van Dokkum, P. G., Labbé, I., et al. 2009, ApJ, 700, 221

Kunth, D., & Östlin, G. 2000, A&A Rev., 10, 1

Lara-López, M. A., Cepa, J., Bongiovanni, A., et al. 2010, A&A, 521, L53

Lequeux, J., Peimbert, M., Rayo, J. F., Serrano, A., & Torres-Peimbert, S. 1979, A&A, 80, 155

Lian, J. H., Li, J. R., Yan, W., & Kong, X. 2015, MNRAS, 446, 1449

Lian, J., Hu, N., Fang, G., Ye, C., & Kong, X. 2016, ApJ, 819, 73

López-Sánchez, Á. R., Dopita, M. A., Kewley, L. J., et al. 2012, MNRAS, 426, 2630

Luo, A.-L., Zhang, H.-T., Zhao, Y.-H., et al. 2012, RAA (Research in Astronomy and Astrophysics), 12, 1243

Luo, A.-L., Zhao, Y.-H., Zhao, G., et al. 2015, RAA (Research in Astronomy and Astrophysics), 15, 1095

Luridiana, V., Morisset, C., & Shaw, R. A. 2015, A&A, 573, A42

Ly, C., Malhotra, S., Malkan, M. A., et al. 2016a, ApJS, 226, 5

Ly, C., Malkan, M. A., Nagao, T., et al. 2014, ApJ, 780, 122

Ly, C., Malkan, M. A., Rigby, J. R., & Nagao, T. 2016b, ApJ, 828, 67

Ly, C., Rigby, J. R., Cooper, M., & Yan, R. 2015, ApJ, 805, 45

Maiolino, R., Nagao, T., Grazian, A., et al. 2008, A&A, 488, 463

Mannucci, F., Cresci, G., Maiolino, R., Marconi, A., & Gnerucci, A. 2010, MNRAS, 408, 2115

Markwardt, C. B., Swank, J. H., Barthelmy, S. D., et al. 2009, The Astronomer's Telegram, 2258, 1

Nicholls, D. C., Dopita, M. A., Sutherland, R. S., et al. 2014, ApJ, 786, 155

Nicholls, D. C., Dopita, M. A., Sutherland, R. S., Kewley, L. J., & Palay, E. 2013, ApJS, 207, 21

Pustilnik, S. A., Kniazev, A. Y., Masegosa, J., et al. 2002, A&A, 389, 779

Pustilnik, S. A., & Martin, J.-M. 2007, A&A, 464, 859

Salim, S., Lee, J. C., Ly, C., et al. 2014, ApJ, 797, 126

Shaw, R. A., de La Pena, M. D., Katsanis, R. M., & Williams, R. E. 1998, in Astronomical Society of the Pacific Conference Series, 145, Astronomical Data Analysis Software and Systems VII, eds. R. Albrecht, R. N. Hook, & H. A. Bushouse, 192

Shaw, R. A., & Dufour, R. J. 1995, PASP, 107, 896

Shi, F., Kong, X., Li, C., & Cheng, F. Z. 2005, A&A, 437, 849

Skillman, E. D., Kennicutt, R. C., & Hodge, P. W. 1989, ApJ, 347, 875

Skrutskie, M. F., Cutri, R. M., Stiening, R., et al. 2006, AJ, 131, 1163

Song, Y.-H., Luo, A.-L., Comte, G., et al. 2012, RAA (Research in Astronomy and Astrophysics), 12, 453

Storey, P. J., Sochi, T., & Badnell, N. R. 2014, MNRAS, 441, 3028

Su, D.-Q., & Cui, X.-Q. 2004, ChJAA (Chin. J. Astron. Astrophys.), 4, 1

Tayal, S. S., & Zatsarinny, O. 2010, ApJS, 188, 32

Tremonti, C. A., Heckman, T. M., Kauffmann, G., et al. 2004, ApJ, 613, 898

Veilleux, S., & Osterbrock, D. E. 1987, ApJS, 63, 295

Wang, S.-G., Su, D.-Q., Chu, Y.-Q., Cui, X., & Wang, Y.-N. 1996, Appl. Opt., 35, 5155

Wright, E. L., Eisenhardt, P. R. M., Mainzer, A. K., et al. 2010, AJ, 140, 1868

Yates, R. M., Kauffmann, G., & Guo, Q. 2012, MNRAS, 422, 215

Zaritsky, D., Kennicutt, Jr., R. C., & Huchra, J. P. 1994, ApJ, 420, 87

Zhao, G., Zhao, Y.-H., Chu, Y.-Q., Jing, Y.-P., & Deng, L.-C. 2012, RAA (Research in Astronomy and Astrophysics), 12, 723